



# Microstructural Characterisation and Hot-Deformation Behaviour of AA6082 Al Alloy Produced by Low-Frequency Electromagnetic Casting

C. Menapace, L. Fioretta, G. Straffellini, L. Canevari, and S. Sannicolò

(Submitted November 28, 2019; in revised form March 13, 2020; published online April 13, 2020)

The present paper outlines the main differences observed in the microstructure and hot workability of AA6082 alloys prepared via low-frequency electromagnetic casting (LFEC) and direct-chill casting, i.e. with and without the application of an electromagnetic stirrer to an innovative casting mould. The hot workability was evaluated through hot-compression tests in the temperature range 450–550 °C and at three different strain rates (0.001, 0.1, and 1 s<sup>-1</sup>). Metallographic analysis revealed a grain-size refinement due to the electromagnetic stirring, accompanied by a change in the extent and type of intermetallic compounds between the dendritic arms. A globular microstructure was observed only in the central part of the LFEC billet, where  $\beta$  intermetallic precipitates were observed. The shape of the true-stress versus true-strain curves indicated the occurrence of a dynamic recovery phenomenon. Although the values of the maximum stress were similar for all the samples, analysis of the hot-compression behaviour through a constitutive model revealed differences in the hot-deformation activation energy  $Q_{HW}$ , with the lowest value belonging to the sample cut from the centre of the LFEC billet, where the effect of stirring was most pronounced.

**Keywords** low-frequency electromagnetic casting, AA6082, hot workability

## 1. Introduction

Most Al alloys for plastic deformation are produced via direct-chill (DC) casting, as reported by different authors (Ref 1–6). DC casting is a semi-continuous vertical casting process in which liquid Al is poured into the top of a mould, which is closed by a bottom block (dummy block), at the beginning of the casting process. Both the dummy block and the mould are cooled by water, which enhances the removal of heat from the liquid metal. (This step is referred to as primary cooling of the ingot.) When the Al starts to solidify, the block is lowered at a constant velocity, which is the casting speed. After removing the ingot from the mould bottom, the solidified metal at the ingot surface is further cooled by water sprays. This cooling process is known as secondary cooling and is clearly described by Sengupta et al. (Ref 7) in a paper on the effect of water cooling on the casting of aluminium. The paper provides an illustration of primary as well as secondary cooling effects on the solidification of Al alloys. After cooling, the ingot is immersed in the water of a casting well, which is positioned approximately 1 m below the mould. When the desired ingot length is reached, the casting process is stopped. (Thus, it is called semi-continuous casting.) Compared with continuous casting, there is a smaller amount of liquid metal in the mould,

which has beneficial effects, such as a more regular solidification front, lower macrosegregation, better microstructural homogeneity, and lower radial stresses, as reported in the book by Eskin (Ref 2), which shows many examples of series 2000, 6000, and 7000 Al alloys that are direct-chill cast.

Although the DC casting process has been improved in the last 20 years, further enhancements can be made to increase the microstructural quality of the ingots. For example, to refine the microstructure, essential to obtain good mechanical properties and reduce the tendency to form pores, a grain refiner, for example, TiB<sub>2</sub> or Al<sub>3</sub>Ti, can be added to the melt (Ref 8–10). Another recently proposed solution is electromagnetic stirring. During solidification, the melt can be stirred using an electromagnetic inductor, which creates a low-frequency electromagnetic field; thus, the melt flow and its temperature distribution can be controlled. Studies have shown the beneficial effects of low-frequency electromagnetic casting (LFEC) for microstructural refinement. The fragmentation of dendrites as the convective fluid flow is moved by the electromagnetic field of the stirrer has been extensively described by Hellawell et al. (Ref 11). Zuo et al. (Ref 12, 13) showed that LFEC induces a higher undercooling in an Al–Zn–Mg–Cu alloy, leading to a higher nucleation rate and a consequent grain-size refinement. The same author (Ref 14) found similar effects of LFEC on an Al–Cu–Mg–Mn alloy. Different authors have studied the influence of LFEC on the casting of Al alloys of the 7XXX series: Zhang B. et al. (Ref 15) found, in a 7075 alloy, a finer and more globular microstructure after LFEC casting, together with reduced Zn and Cu macrosegregation; the same author also studied the effect of the frequency applied; Chen et al. (Ref 16) found similar results on the same alloy with a lower microsegregation of Cu, Mg, and Zn among the dendrites; and lastly Zhang H. et al. (Ref 17) described the mechanism responsible for grain refinement and lower segregation through a model and compared the results with experimental data on the same class of Al alloys. The main

C. Menapace, L. Fioretta, and G. Straffellini, Department of Industrial Engineering, University of Trento, Trento, Italy; L. Canevari, Almec srl, Rovereto, TN, Italy; and S. Sannicolò, Bolzano, Italy. Contact e-mail: cinzia.menapace@unitn.it.

purpose of the stirring is to produce high-quality ingots that have a fine homogeneous globular microstructure with limited segregation (sub-cortical and axial). Equiaxed grains in casting products can form due to either a heterogeneous nucleation (external source) or dendrite fragments, which act as an internal source of nucleation. In the absence of external nucleants, fragments of dendrite are the major sources of equiaxed grain formation, as described by Hao et al. (Ref 18) for an electromagnetically cast 2024 aluminium alloy. The same results were found by Zhao et al. (Ref 19), who studied the same alloy cast under LFEC. On the same topic, Zuo et al. (Ref 20) showed a finer and more globular microstructure obtained through electromagnetic casting in an Al–Zn–Mg–Cu alloy with consequent better tensile properties. Recently, LFEC has also been applied to Al–Li alloys (Ref 21). The microstructural improvements obtained through this technology also have beneficial effects on industrial productivity, since the subsequent plastic-deformation processes (such as extrusion) require lower forces. Moreover, homogenisation treatment, which is often used for Al alloys to reduce segregation and induce microstructural globularisation, can be significantly reduced or even eliminated, saving time, and reducing costs. To this end, LFEC has been applied to AA 6082 alloy, which in the last few decades has gained increasing interest since it is reasonably strong considering its low alloying element content, as well as being formable, corrosion resistant, and weldable. It now occupies a significant part of the market, replacing AA6061 in many applications (Ref 4). This alloy is typically used in highly stressed applications, such as trusses, bridges, transport applications, barrels, and automotive components such as wheel rims. No literature data have been found on the application of LFEC to this alloy.

Since AA6082 is mainly transformed by warm plastic-deformation processes (such as extrusion, forging or deep drawing) to obtain parts with either simple or complex geometry, the analysis of its hot workability is of primary importance. This is frequently done by means of hot compression tests, analysing the stress–strain curves, and the microstructures obtained after deformation. Different alloy families show very different hot compression curves, which depend on the parameters used (i.e. temperature and strain rate) (Ref 22–28). These curves can be classified into four main types: (1) continuous flow softening after a peak stress, (2) flat stress–strain curves indicating a steady-state flow behaviour, (3) a rapid drop in flow stress after a single peak, which normally indicates the occurrence of dynamic recrystallisation, (4) an oscillating curve indicating plastic flow instability. During hot deformation of aluminium alloys, dynamic recovery is more likely to happen than recrystallisation because of the high stacking fault energy of aluminium (Ref 29). Thus, the objective of the present study was to apply LFEC to AA6082 alloy and analyse its microstructure and hot workability, evaluated using hot-compression tests, comparing them with those of the same alloy cast via the conventional DC method.

## 2. Experimental Procedure

Round billets (330 mm in diameter) were produced via conventional DC casting with and without the use of an electromagnetic stirrer. Table 1 presents the composition of the AA6082 alloy, measured through a quantometer ARL 3560 OES in accordance with the standard ASTM A751-14. The alloy was cast in six parallel billets (3-m long)—three without stirring and three with stirring—using the same casting parameters. The technical characteristics of the stirrer installed on the DC casting machine, manufactured by Ergolines s.r.l. (Italy), such as the geometry, current, number of coils, and rotation frequency, cannot be revealed, owing to a confidentiality agreement.

Sections of the billets cast via the conventional method and using a stirrer were cut in the middle of the billet length. Across the section, samples for metallographic analysis and hot-compression tests were cut from three different positions (centre = C, middle radius = M, external crown = R), as shown in Fig. 1. The samples cut from the billet cast with stirring are denoted as CS, MS, and RS.

For the metallographic analysis, the samples were etched with a solution of nitric acid, hydrofluoric acid, and chromium trioxide in distilled water and examined using a light optical microscope and a scanning electron microscope. On the metallographic samples, dendrite arm spacing (DAS) was also measured. This is a parameter commonly used to describe cast microstructural fineness, defined as the distance between the dendrites' secondary arms. (Therefore, it is also known as SDAS, i.e. secondary dendrite arm spacing). Dendrite arm spacing was measured through an image analysis system, applying the linear line intercept method. In this method, a line

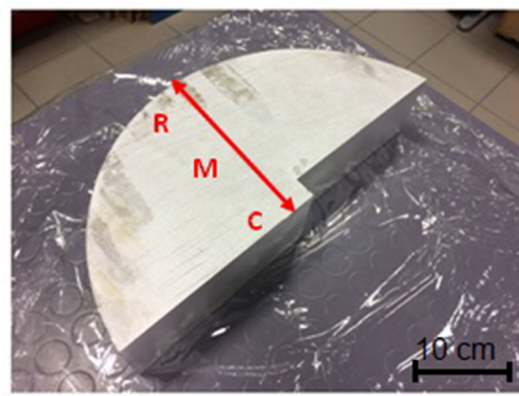


**Fig. 1** Billet section and positions from which the R, M, and C samples were cut. The constant  $n$  is the mean slope of the  $\ln \dot{\epsilon}$  vs.  $\ln(\sinh(\alpha\sigma))$  line (Fig. 13a). The activation energy can be expressed as  $Q_{HW} = nRs$ , where  $s$  is the slope of the  $\ln(\sinh(\alpha\sigma))$  vs.  $1000/T$  line (Fig. 13b), and was derived for the four materials under investigation

**Table 1** Chemical composition of the AA6082 cast alloy (wt.%)

Si	Mn	Mg	Fe	Cu	Zn	Ti	Cr	Ni	Pb	Al
1.2449	0.6780	1.0955	0.4273	0.0756	0.0547	0.0854	0.1616	0.0106	0.0107	Bal.



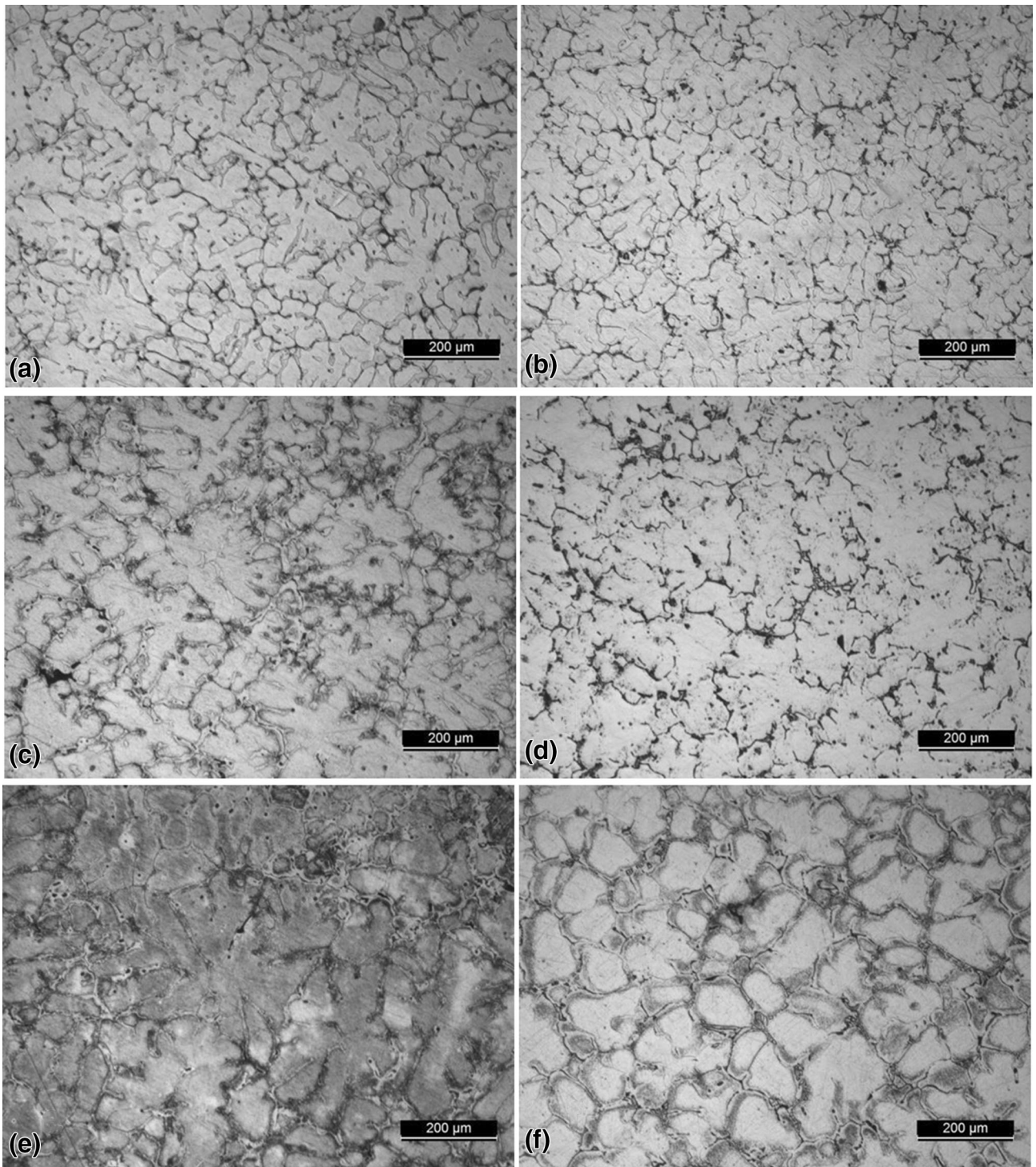


**Fig. 2** Microstructures of samples cast without stirring (a) R, (c) M, (e) C and with electromagnetic stirring (b) RS, (d) MS, (f) CS

**Table 2** dendrite arm spacing (DAS) of the samples, in  $\mu\text{m}$

Dendrite arm spacing DAS ( $\mu\text{m}$ )					
R	RS	M	MS	C	CS
$33.3 \pm 1.2$	$30.8 \pm 1.5$	$41.5 \pm 1.9$	$36.4 \pm 1.6$	$63.7 \pm 2.1$	$50.2 \pm 1.9$

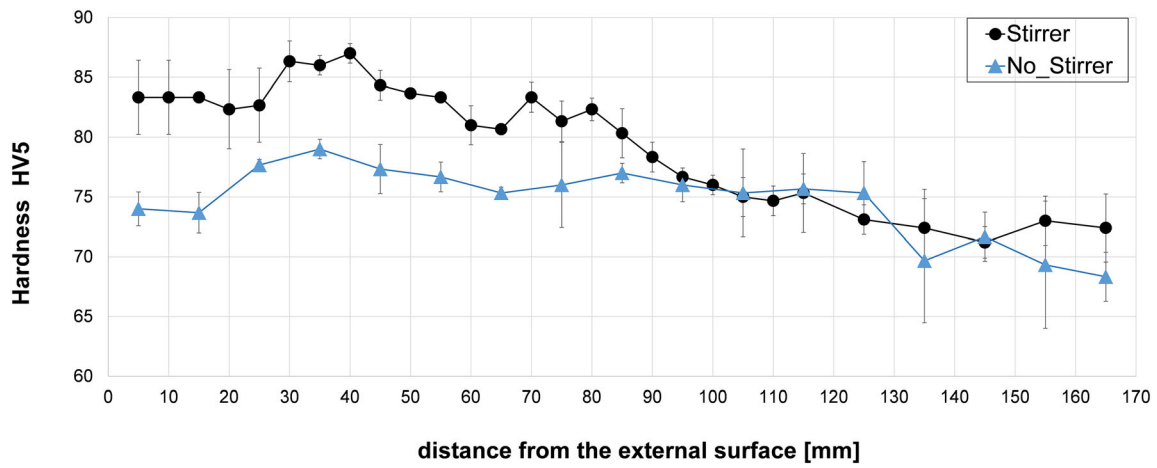


Fig. 3 HV5 hardness profiles of conventionally DC-cast and LFEC billets

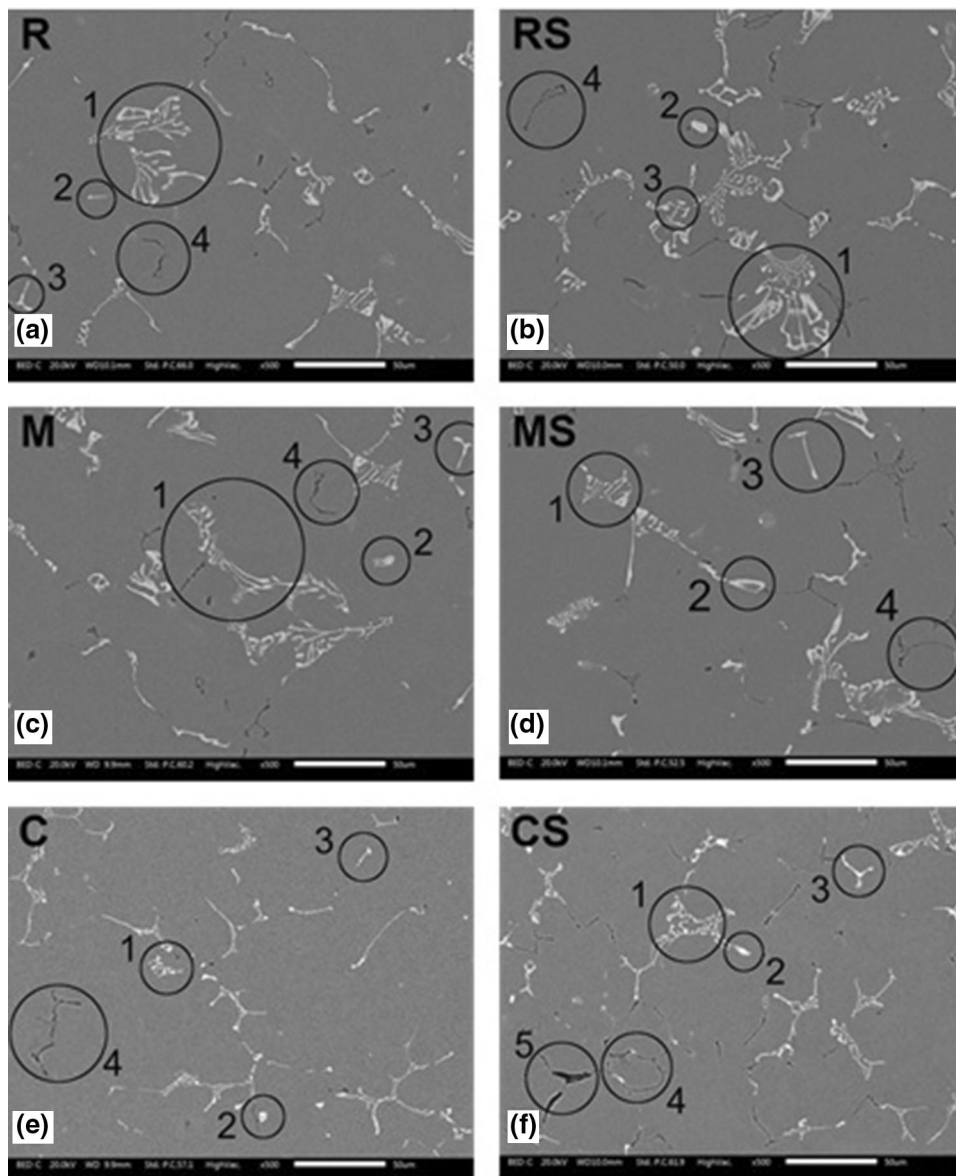
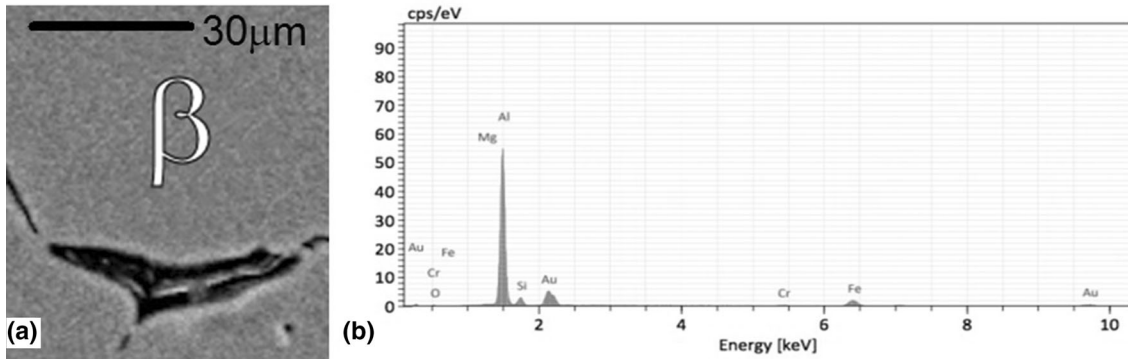
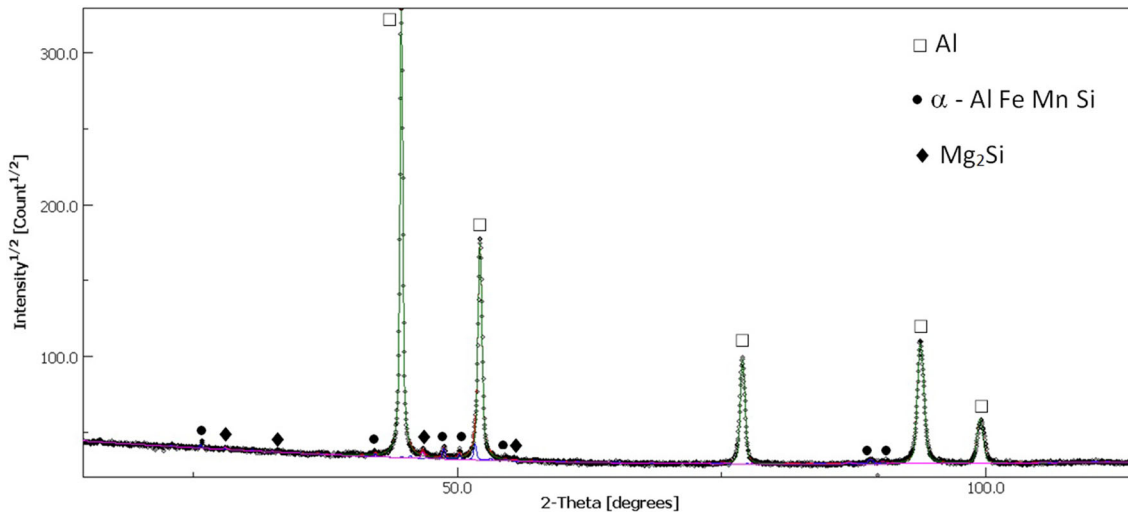


Fig. 4 SEM micrographs of samples (a) R, (b) RS, (c) M, (d) MS, (e) C, and (f) CS. Examples of intermetallics are indicated as follows: (1)  $\alpha$ -Al(FeMn)Si-Chinese script, (2)  $\alpha$ -Al<sub>15</sub>(FeMn)<sub>3</sub>Si-platelet, (3)  $\alpha$ -Al(FeMn)Si T-bone, (4) Mg<sub>2</sub>Si, and (5)  $\beta$ -Al<sub>5</sub>FeSi



**Fig. 5** SEM micrograph detail of  $\beta$  intermetallic detected in sample CS (a) and its relative EDS analysis (b)



**Fig. 6** XRD pattern of sample CS

of length  $L$  is drawn along the principal arm of a dendrite and the number of secondary arms crossing this line is counted (Crepeau et al. in Ref 30). DAS is obtained dividing  $L$  by the number  $n$  of secondary arms crossed by the line.

In order to investigate the microstructure of the cast samples, X-ray diffraction (XRD) measurements were carried out with an IPD3000 diffractometer equipped with a Co anode source (line focus), a multilayer monochromator to suppress  $k$ -beta radiation and fixed 100  $\mu\text{m}$  slits. The sample was positioned in reflection geometry with a fixed omega angle with respect to the incident beam (typically 5°); diffraction data were collected by means of an Inel CPS120 detector over the 5°-120° 2-theta range (0.03° per channel); acquisition time was as low as 10 min for quick qualitative evaluation and up to 1 h for quantitative/Rietveld analysis.

Additionally, differential thermal analysis (DTA) was performed up to 650 °C using a Netzsch STA Luxx 409 apparatus in an inert atmosphere to investigate the incipient melting of the alloy.

Hot-compression tests were performed using a horizontal Bähr dilatometer DIL 805A/D equipped with a hydraulic

system able to apply a compression force through two alumina punches. The samples were cylinders with a diameter of 5 mm and a height of 10 mm. Pure Mo discs (99.95 wt.% Mo) with a thickness of 0.1 mm and a diameter of 8 mm were arranged between the cylindrical sample and the punches to reduce friction and increase the thermal barrier effect. The specimens were heated through a copper inductor, and their temperature was recorded by means of a Pt:Pt-Rh thermocouple. High vacuum ( $10^{-4}$  mbar) was applied in the chamber during the tests to reduce the surface oxidation. The compression-test temperatures were selected to cover the typical range for hot working of AA6082 alloy, i.e. 450, 500, and 550 °C. Three deformation rates were used: 0.001, 0.1, and 1  $\text{s}^{-1}$ . Before compression, the samples were held at the deformation temperature for 5 min in order to ensure a uniform temperature distribution in the whole specimen. All tests were performed up to a maximum true strain of 0.5. After the tests, the deformed samples were cooled at 10 °C/s with a flux of inert gas to “freeze” the microstructure for the subsequent metallographic investigations.



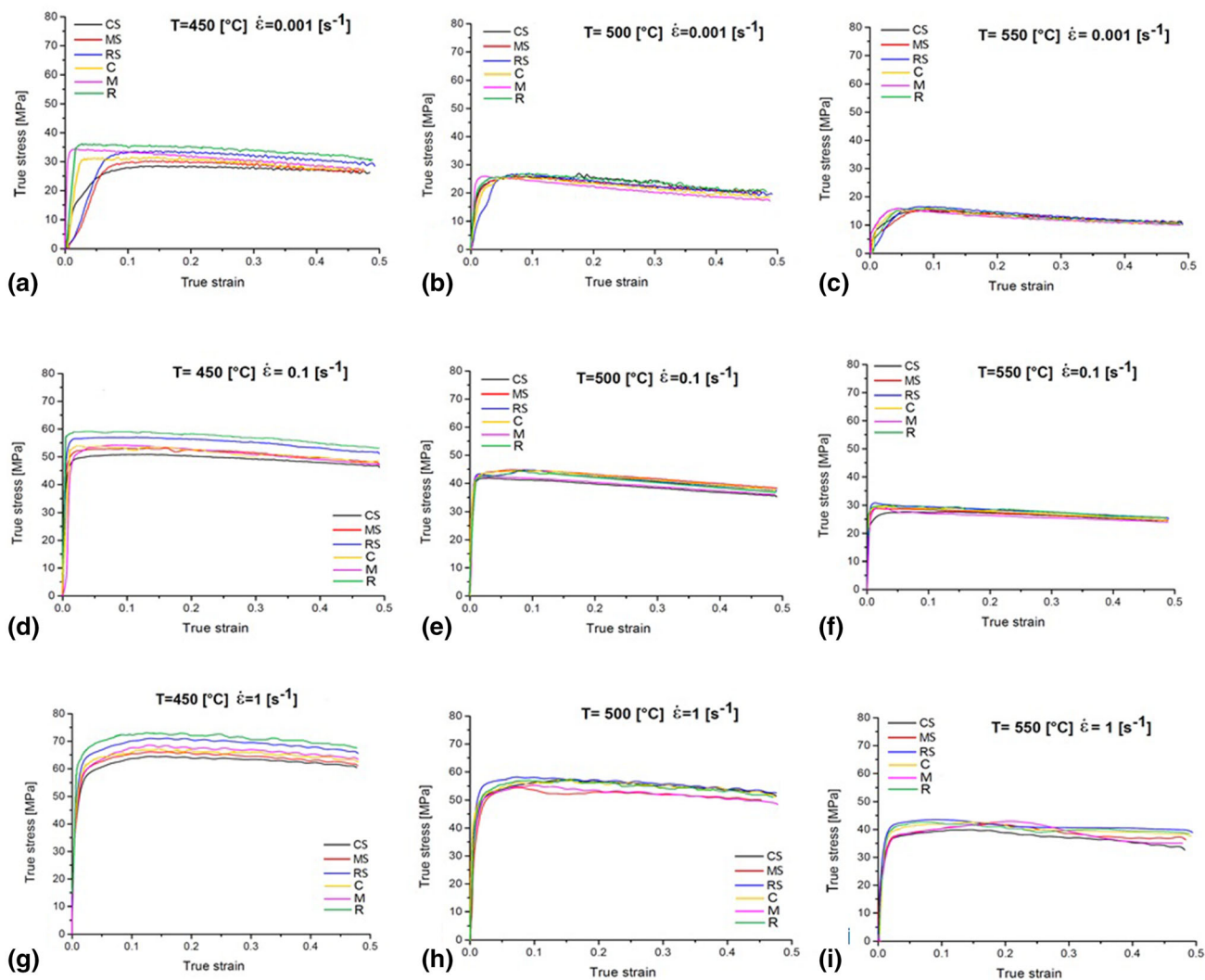


**Fig. 7** Hot-compression curves of samples CS, MS, RS and C, M, R under different temperature and strain rate conditions: (a)  $T = 450\text{ }^{\circ}\text{C}$ — $\dot{\epsilon} = 0.001\text{ s}^{-1}$ , (b)  $T = 500\text{ }^{\circ}\text{C}$ — $\dot{\epsilon} = 0.001\text{ s}^{-1}$ , (c)  $T = 550\text{ }^{\circ}\text{C}$ — $\dot{\epsilon} = 0.001\text{ s}^{-1}$ , (d)  $T = 450\text{ }^{\circ}\text{C}$ — $\dot{\epsilon} = 0.1\text{ s}^{-1}$ , (e)  $T = 500\text{ }^{\circ}\text{C}$ — $\dot{\epsilon} = 0.1\text{ s}^{-1}$ , (f)  $T = 550\text{ }^{\circ}\text{C}$ — $\dot{\epsilon} = 0.1\text{ s}^{-1}$ , (g)  $T = 450\text{ }^{\circ}\text{C}$ — $\dot{\epsilon} = 1\text{ s}^{-1}$ , (h)  $T = 500\text{ }^{\circ}\text{C}$ — $\dot{\epsilon} = 1\text{ s}^{-1}$ , (i)  $T = 550\text{ }^{\circ}\text{C}$ — $\dot{\epsilon} = 1\text{ s}^{-1}$

### 3. Results and Discussion

#### 3.1 Microstructures

The microstructures of samples taken from the billets cast with and without stirring are presented in Fig. 2a–f. The microstructures were dendritic for all the samples, except for CS, which clearly exhibited a globular structure. The microstructures of the billet cast with the stirrer (S) exhibited finer grains. In both billets, the grain size was small in the external crown (R) and increased towards M and C, as can be observed from the dendrite arm spacing (DAS) measured on the three samples and reported in Table 2. The dendrites were surrounded by a network of intermetallics (which appear as dark regions in the micrographs of Fig. 2).

The hardness profiles (HV5) measured along the radius of both billets are shown in Fig. 3. The difference in hardness was approximately 10 HV in the R region. It was reduced in the M zone and disappeared in the centre. The higher hardness of the RS and MS samples was due to the finer grains, whereas in CS, even though the grain size is smaller, the Al matrix micro-

hardness is much lower than in the external layer of the billet. It decreased from 76 HV<sub>0.05</sub> in RS to 71 HV<sub>0.05</sub> in MS, down to 51 HV<sub>0.05</sub> in the CS sample. This difference, due to a depletion in solid solution alloying elements in the matrix, accounts for the CS sample having a hardness level similar to the C sample.

Scanning electron microscopy (SEM) analysis of the samples indicated the presence of different types of intermetallics. The most abundant intermetallic in all the specimens was  $\alpha\text{-Al}_{15}(\text{FeMn})_3\text{Si}$ , with Chinese script (number 1 in all the micrographs of Fig. 4), platelet (number 2), and T-bone (3) morphologies. In addition to  $\alpha$ , there were  $\text{Mg}_2\text{Si}$  precipitates (number 4 in Fig. 4). In the CS sample,  $\beta\text{-Al}_5\text{FeSi}$  particles were detected, as shown in Fig. 4 (precipitate number 5) and in detail in Fig. 5 with its EDXS analysis.  $\beta$  precipitates can form through a eutectic or peritectic reaction. Both the eutectic reaction  $L \rightarrow \alpha\text{-Al} + \beta\text{-Al}_5\text{FeSi}$  and the peritectic reaction  $L + \alpha\text{-AlFeSi} \rightarrow \alpha\text{-Al} + \beta\text{-Al}_5\text{FeSi}$  occurs at a slow cooling rate ( $2\text{ }^{\circ}\text{C}/\text{min}$ ) during casting as observed by Mrówka-Nowotnik et al. (Ref 31). These reactions occur when the eutectic composition is reached at the interaction front. Liu et al. (Ref 32), studying the solidification process of this alloy,

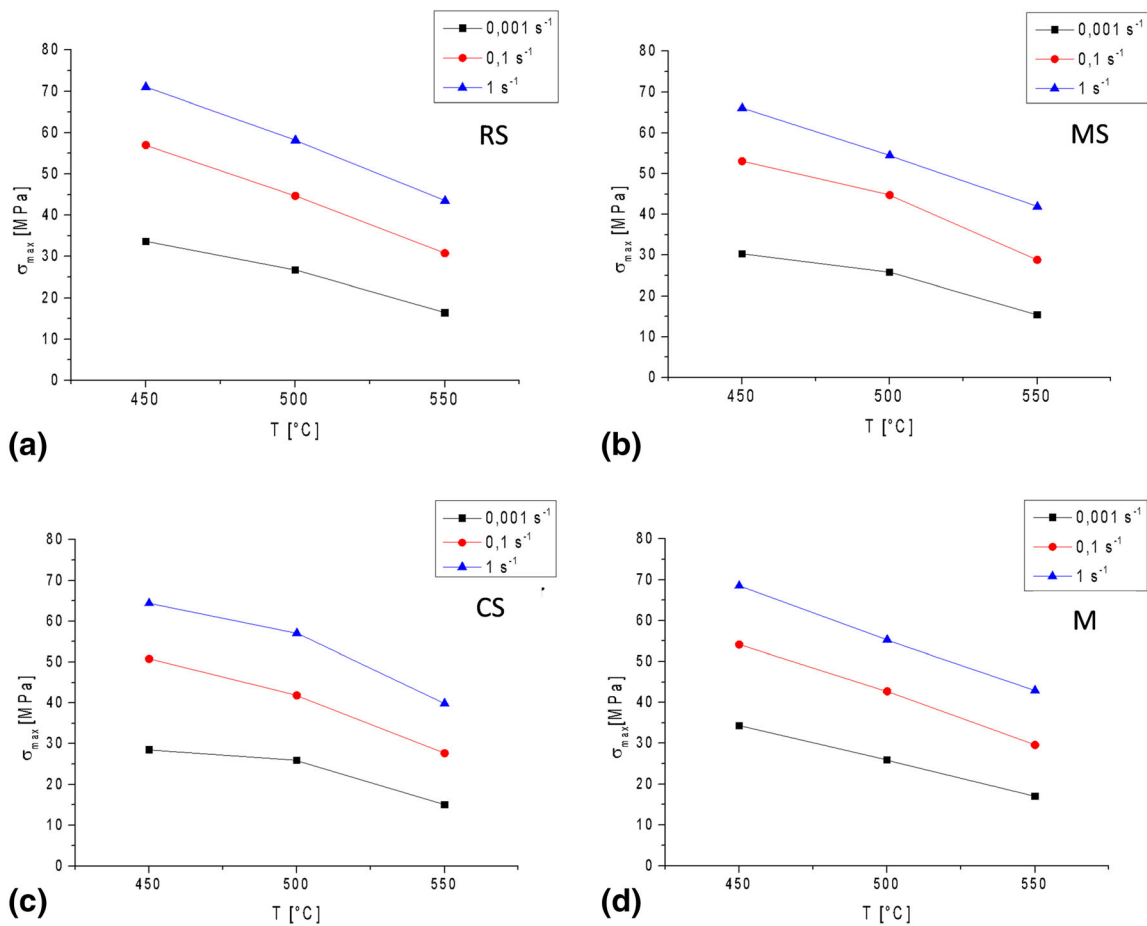


**Fig. 8**  $\sigma_p$  with respect to the temperature and strain rate for (a) RS, (b) MS, (c) CS, and (d) M

indicated that the precipitation temperature of the  $\beta$ -Al<sub>5</sub>FeSi intermetallic was approximately 570 °C, which corresponds to 10% of the liquid. This intermetallic generally precipitates in the interdendritic regions in the form of thin plates. Because it is formed only when the eutectic composition is reached, the stirring is considered to enrich the Fe in the central part of the billet through the complex movements of the solute-rich liquid. Ahmedein et al. (Ref 33) highlighted the importance of thermal and solutal flows together with the movements of the equiaxed grains into the solidifying liquid in order to determine the amount of alloying element segregation. The Fe enrichment in the central part was confirmed by the chemical analysis of the Fe content in the RS, MS, and CS samples and showed an increase in Fe wt.% from 0.38 in RS, to 0.41 in MS, and up to 0.56 in CS. This enrichment is the result of different factors, such as the low solubility of Fe in the  $\alpha$ -Al matrix, the relatively high density of Fe compared with that of the other alloying elements (which influences the liquid flow through gravity, as explained by Hellawell et al. in Ref [11]), and stirrer parameters, such as current intensity and frequency. Zhang et al. (Ref 15) and Chen et al. (Ref 16) studied the influence of these two parameters on the distribution of alloying elements in the billet section of a 7075 Al alloy. An in-depth investigation of Fe-rich precipitate formation was carried out by Hsu et al. (Ref 34) through differential scanning calorimetry (DSC) and transmission electron microscopy (TEM) observations; the authors detected two different morphological forms of the

precipitate  $\alpha_c$ -AlFeSi, depending on the way it is formed, i.e. through a peritectic or a eutectic reaction.

XRD analysis, carried out on the six samples, showed no difference between the specimens. All spectra show the peaks of Al and very small peaks corresponding to  $\alpha$ -Al(FeMn)Si and Mg<sub>2</sub>Si. As an example, Fig. 6 shows the XRD spectrum of the CS sample. The amount of  $\alpha$  intermetallic measured was  $\sim 1.5\%$ , and Mg<sub>2</sub>Si  $\sim 0.5\%$ , whereas  $\beta$ -Al<sub>5</sub>FeSi was not detected by XRD because the amount was too low.

### 3.2 Hot Compression

The true stress–true strain curves of the CS, MS, and RS samples, as well as M, which is considered representative of the conventional casting process, are shown in Fig. 7. For all the samples, the flow stress initially increases with the strain, reaches a maximum (peak stress  $\sigma_p$ ), and then slowly decreases (at strain rates of 0.001 and 0.1  $s^{-1}$ ) or stabilises, forming an almost constant plastic flow stress (at the highest strain rate of 1  $s^{-1}$ ). This curve shape suggests the occurrence of dynamic recovery (DRV), which is typical of high-stacking fault energy alloys such as Al alloys, as stated by McQueen (Ref 35). The slight continuous decrease at the lower strain rates may be associated with a softening process due to the plastic-deformation response of the samples under a constant load at a high temperature for a certain time (5 s in the case of  $\dot{\epsilon} = 0.1 s^{-1}$  and 500 s in the case of  $\dot{\epsilon} = 0.001 s^{-1}$ ). Flow softening is due both to heating effects produced by the deformation and to

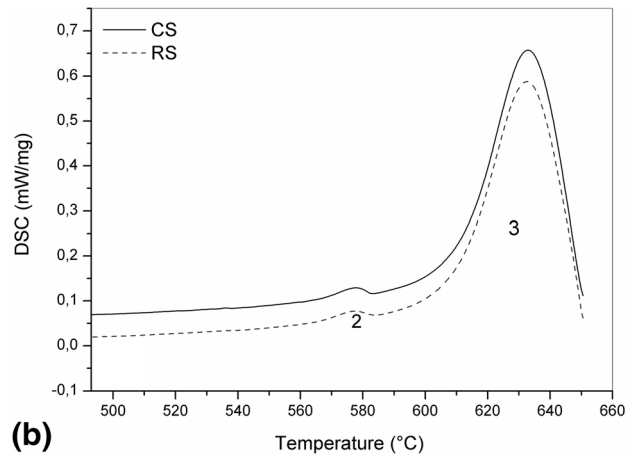
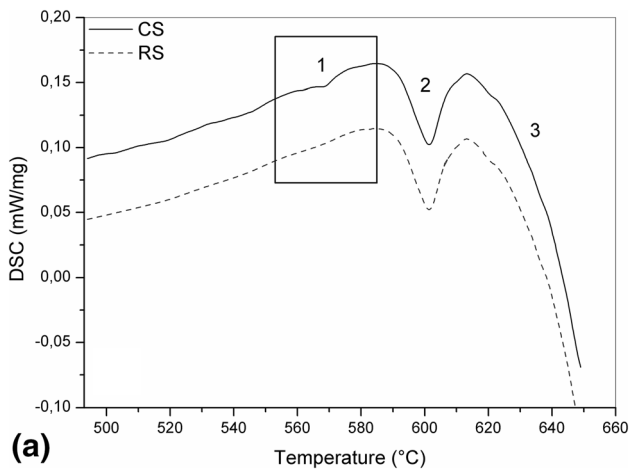


**Fig. 9** DTA curves of the CS and RS samples: (a) heating step; (b) cooling step

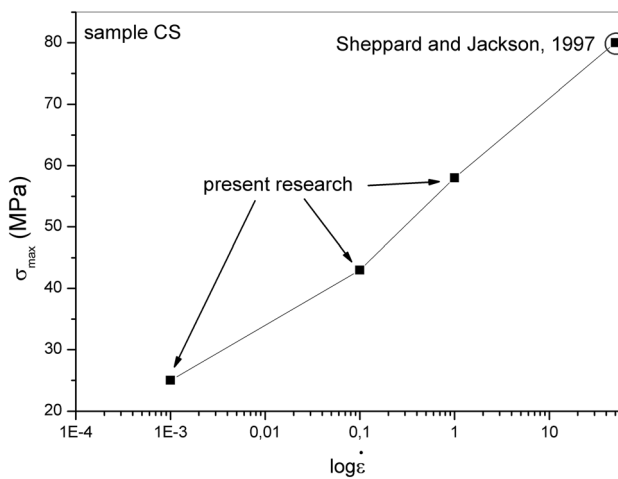


**Fig. 10** Maximum flow stress ( $\sigma_{max}$ ) as a function of the strain rate (in log scale) used for the hot compression tests

microstructural changes, which lead to a progressive stress decrease, as described by Sakai et al. (Ref 36). In an extensive review paper, Lin et al. (Ref 37) widely described the hot

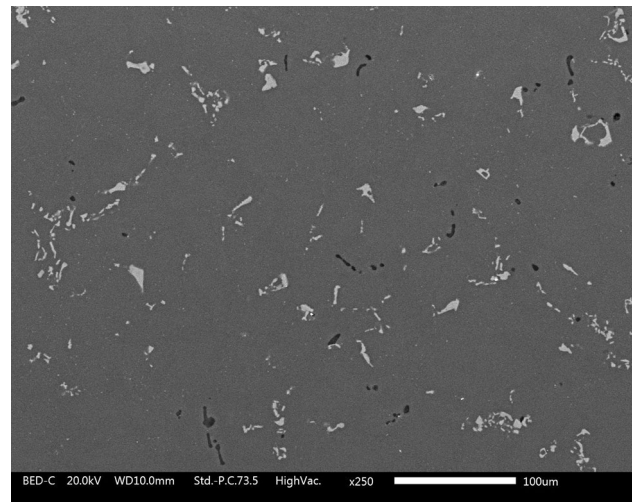
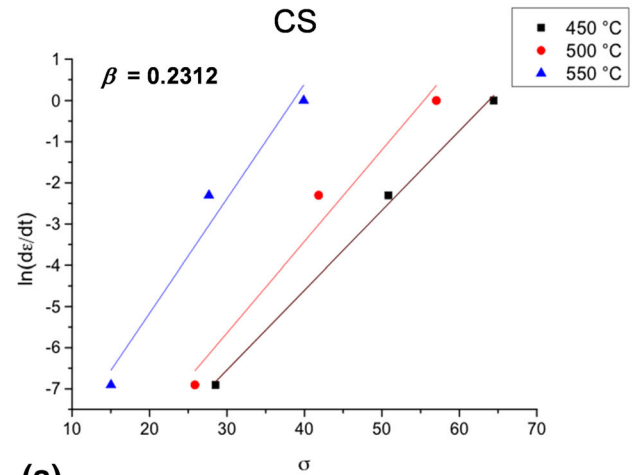
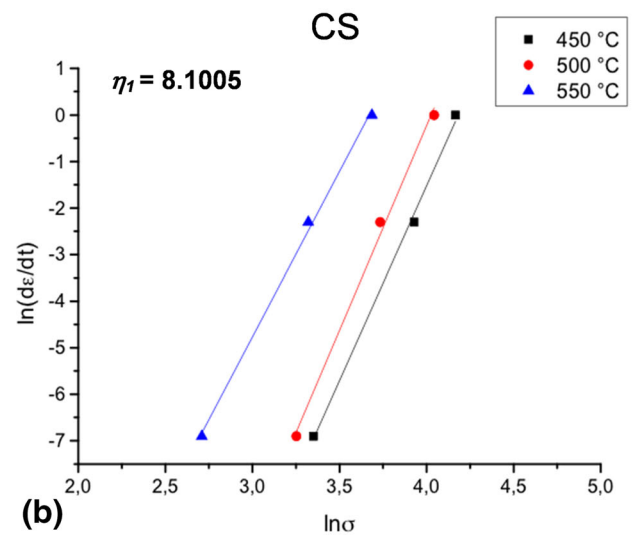


**Fig. 11** SEM micrograph of the CS sample after deformation at 550 °C and 1 s<sup>-1</sup>



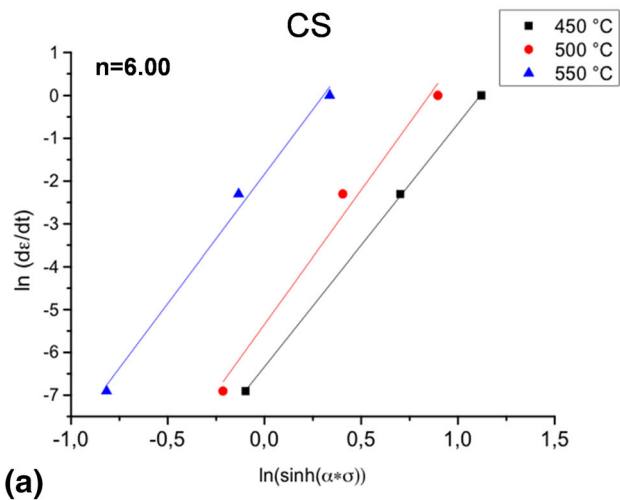
**(a)**



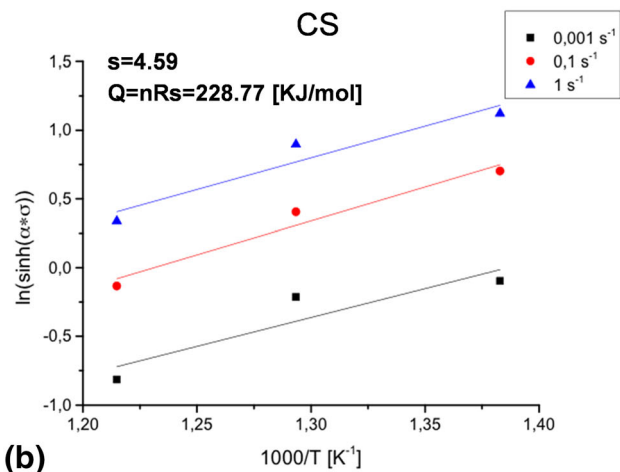
**(b)**

**Fig. 12** (a)  $\ln \dot{\epsilon}$  vs.  $\sigma$  and (b)  $\ln \dot{\epsilon}$  vs.  $\ln \sigma$  correlations for the CS sample





(a)



(b)

**Fig. 13** (a)  $\ln \dot{\epsilon}$  vs.  $\ln(\sinh(\alpha\sigma))$  and (b)  $\ln(\sinh(\alpha\sigma_p))$  vs.  $1000/T$

workability behaviour of different alloys (ferrous and non-ferrous) at different temperature and strain rates.

As can be seen in Fig. 6, under all the test conditions, the curves did not indicate a rapid stress drop that is typically observed in the case of the dynamic recrystallisation of Al alloys, as shown by Sakai et al. (Ref 36) and Quan et al. (Ref 38) on 7075 alloy.

As expected, as the test temperature increased, the flow stress decreased, and as the strain rate increased, the stress increased. The deformation ( $\epsilon_p$ ) associated with the peak stress ( $\sigma_p$ ) changed with the temperature and the strain rate; i.e. it increased and decreased with an increase in the strain rate and temperature, respectively. Among the four samples analysed in the present research, no differences were observed, except at the lowest temperature (450 °C). At 450 °C, the LFEC specimens exhibited a difference, with the CS sample showing the lowest stress values, which is attributed to its globular microstructure with a less interconnected intermetallic network and also a lower matrix microhardness.

The peak flow stress  $\sigma_{\max}$  with respect to the temperature and strain rate is shown in Fig. 8a–d for RS, MS, CS, and M, respectively. For all the samples, an almost linear decrease in the maximum flow stress was observed as temperature increased within the tested temperature range.

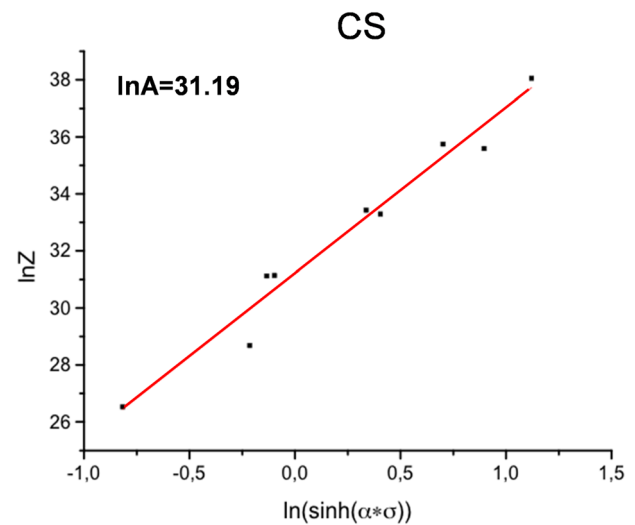


**Fig. 14** Zener–Hollomon parameter ( $Z$ ) as a function of  $(\sinh(\alpha\sigma_p))$  in logarithmic scale, used to determine the value of the constant  $A$ , according to the formula (2)

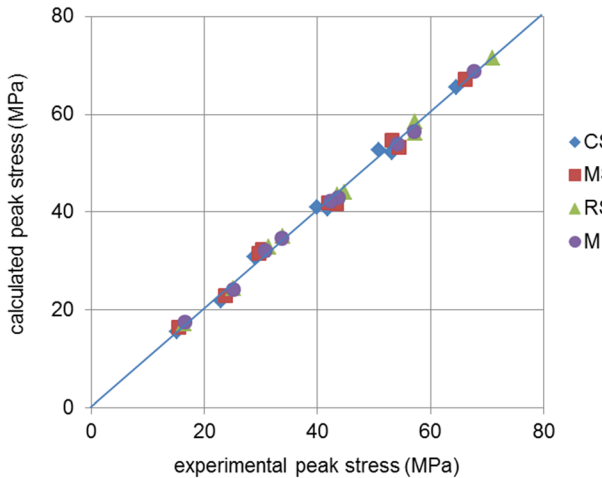
The decrease in  $\sigma_{\max}$  with the increasing temperature exhibited an almost linear trend, with a constant slope between 450 and 550 °C. However, the CS sample showed a slope change between 500 and 550 °C, with a significant drop in  $\sigma_{\max}$ . This is probably related to its microstructure, which was more sensitive to a temperature increase near the  $T_{\text{liquidus}}$ . The presence of a small quantity of low-melting point intermetallic  $\beta\text{-Al}_3\text{FeSi}$ , which melts around 570 °C as shown by Liu et al. (Ref 32), in the CS sample may have led to local liquid-phase formation, as this melting point is close to the nominal temperature used for testing. To investigate this, DTA was performed. The obtained curve for the CS sample is shown in Fig. 9a. It exhibits a small endothermic peak at 568 °C (peak 1), which could be associated with the reaction  $\alpha\text{-Al} + \beta\text{-Al}_3\text{FeSi} \rightarrow \text{L} + \alpha\text{-AlFeSi}$ . This peak is not present in the curve of the RS sample, as shown in the inset comparing this part of the CS and RS curves. Peak 2 corresponds to the melting of most of the intermetallics present in this alloy ( $\alpha$  type), which were observed to melt at 590 °C, while the complete melting of the Al matrix was detected at 615 °C (beginning of endothermic peak 3). Figure 9b shows the DTA curves recorded during the cooling step: solidification peaks 2 and 3 are visible, corresponding to peaks 2 and 3 in the heating, respectively, and peak 1 disappeared. The  $\beta$  intermetallic solubilised into the Al matrix after melting and did not reprecipitate upon cooling.

$\sigma_{\max}$  can be expressed as a function of  $\dot{\epsilon}$ . In the log scale, this leads to the correlation shown in Fig. 10. The data of the present study are in accordance with those of Sheppard and Jackson (Ref 39), who reported for the as-cast AA6082 alloy a flow stress of 80 MPa at a strain rate of  $50 \text{ s}^{-1}$  and a temperature of 500 °C.

Figure 11 shows an SEM micrograph of the CS sample deformed at 550 °C and  $1 \text{ s}^{-1}$ . In this sample, a less continuous network (compared with that of the initial sample, shown in Fig. 4) comprising only  $\alpha$  intermetallics was observed. No traces of  $\beta$  particles were detected, confirming the absence of this precipitate in the CS sample after the hot-deformation step at 550 °C, which was due to the melting and solubilisation into the Al matrix during the test.

**Table 3** constants of the constitutive model of Eq 1

	$\beta$	$\eta_1$	$\alpha$ , MPa <sup>-1</sup>	$N$	$s$	$Q_{HW}$ , kJ/mol	$A$ , s <sup>-1</sup>
CS	0.2312	8.1005	0.0286	6.00	4.59	229	3.53E+13
MS	0.2319	8.2392	0.0281	6.12	4.66	237	1.10E+14
RS	0.2213	8.3881	0.0264	6.21	4.90	253	1.33E+15
M	0.2355	8.8826	0.0265	6.59	4.72	259	3.71E+15

**Fig. 15** Calculated  $\sigma_p$  vs. experimental  $\sigma_p$ 

### 3.3 Development of Constitutive Model

The peak stress,  $\sigma_p$ , can be correlated to the temperature and strain rate via different equations proposed in the literature by Sellars (Ref 40, 41) and Mc Queen (Ref 35, 42). One of the most commonly used equations is the hyperbolic sin-type equation proposed for the first time by Sellars and McTegart (Ref 43) (Eq 1).

$$Z = \dot{\epsilon} \exp\left(\frac{Q_{HW}}{RT}\right) = A(\sinh \alpha \sigma)^n \quad (\text{Eq 1})$$

Here,  $Z$  is the Zener–Hollomon parameter,  $A$  and  $n$  are constants,  $R = 8.314 \text{ J mol}^{-1} \text{ K}^{-1}$  is the universal gas constant,  $Q_{HW}$  is the activation energy of the process (kJ/mol), and  $\alpha = \beta/\eta_1$  is a constant called the stress multiplier. The coefficient  $\beta$  is the mean slope of the  $\ln \dot{\epsilon}$  versus  $\sigma$  lines, as shown in Fig. 12a for the CS sample, and  $\eta_1$  represents the mean slope of the  $\ln \dot{\epsilon}$  versus  $\ln(\sigma)$  line, as shown in Fig. 12b.

Among all the constants,  $Q_{HW}$ , i.e. the energy of plastic deformation in the steady state, is the most important because it represents the energy barrier that must be exceeded in order to start the plastic-deformation process. Actually, in the present work, the steady state is only momentarily achieved, and therefore, these considerations can be valid and applicable only in this range of strain.  $Q_{HW}$  depends on the chemical composition and microstructure; for example, in steel, it increases with the concentration of solutes, precipitates, and inclusions, which prevent and slow down the dislocation movement.

The last constant to be determined was  $A$ , which can be calculated by applying the natural log to Eq 1, yielding Eq 2.

The value of  $\ln A$  is derived by plotting  $\ln Z$  versus  $\log(\sinh(\alpha\sigma))$  (Fig. 14) and measuring the intercept with the  $y$  axis.

$$\ln Z = \ln A + n * \ln[\sinh(\alpha\sigma_p)] \quad (\text{Eq 2})$$

The constants determined for all the samples using this method are presented in Table 3.

Among the samples analysed, CS exhibited the lowest  $Q_{HW}$  value, as it was characterised by a globular microstructure with a less interconnected network of interdendritic precipitates; i.e. the microstructure was more easily deformed. The RS and M samples exhibited the highest activation energies, owing to their highly dendritic microstructure with extended intermetallic networks that acted as barriers for the dislocation motion. Moreover, the decrease in the hardness of the billet cast with stirring from the external radius towards the centre (RS  $\rightarrow$  MS  $\rightarrow$  CS) is reflected by the decrease in  $Q_{HW}$ , in agreement with previous studies, in which a low hardness was associated with a small amount of solutes and precipitates. This correlation between  $Q_{HW}$  and chemical composition was shown by Medina and Hernandez (Ref 44) in low-alloyed steels, by Siyasiya and Stumpf (Ref 45) in Mn steels and also by the author in four different commercially available steels (Ref 46). This behaviour has also been observed for differently treated AA6082 alloys. For a T6 heat-treated AA6082 alloy, Spigarelli et al. (Ref 47) reported an activation energy of 269 kJ/mol. As explained by these authors, high values of the activation energy, significantly higher than the activation energy for self-diffusion in Al (143 kJ/mol), are frequently observed for heat-treated alloys and are related to the presence of precipitates. Accordingly, Zhang et al. (Ref 48) reported an activation energy of 200 kJ/mol for annealed AA6082 hot compressed in the temperature range 300–500 °C, with strain rates of 0.005, 0.05, and 0.09 s<sup>-1</sup>. Other Al alloys, such as 7075, whose hot workability was analysed by Quan et al. (Ref 38) and 7050, studied by Wang et al. (Ref 49), exhibit a wide range of  $Q_{HW}$  depending on the temperature and strain rate at which they are hot-compressed, since both of these parameters influence the microstructure, and therefore, the hot workability of these alloys. The constants of Table 3 can be substituted into the Eq 3, which was derived from Eq 1, yielding the constitutive equations for the four materials.

$$\epsilon^1 = A(\sinh(\alpha\sigma_p))^n \exp\left[-\left(\frac{Q_{HW}}{RT}\right)\right] \quad (\text{Eq 3})$$

Comparing the data obtained from these equations with the experimental data, a good agreement is found as illustrated in Fig. 15, where calculated  $\sigma_p$  versus experimental  $\sigma_p$  is shown. The maximum difference observed is < 6%.

## 4. Conclusions

The microstructural analysis and the investigation of the hot workability of AA6082 alloys DC-cast via a conventional method and with an electromagnetic stirrer led to the following conclusions.

- There was a grain-size refinement along the whole radius of the billet cast with low-frequency electromagnetic stirring. The electromagnetic stirring induced liquid–metal mixing, leading to the formation of Fe-rich  $\beta$ -Al<sub>5</sub>FeSi in the central part of this billet (CS sample).
- The grain refinement led to higher hardness in the external parts of the billet cast with the stirrer.
- The hot-compression curves obtained at three different temperatures (450, 500, and 550 °C) and three different strain rates (0.001, 0.1, and 1 s<sup>-1</sup>) exhibited similar trends for the billets cast with and without stirring. The shapes of these curves, together with the metallographic analysis of the samples after the deformation tests, indicated the occurrence of a DRV phenomenon after the peak stress  $\sigma_p$  was reached. The peak stress increased with the strain rate and decreased with an increase in temperature.
- The correlations among the maximum plastic flow, strain rate, and temperature during the isothermal hot compression were described by an Arrhenius-type equation. A constitutive model describing the deformation behaviour of samples cast with and without stirring was developed. From this model, the activation energy ( $Q_{HW}$ ) was derived, which exhibited lower values for LFEC samples, particularly for the CS sample, in which the globular microstructure was accompanied by a lower hardness.
- Because it is desirable to achieve the microstructure of the CS sample in the whole billet section, future research will be carried out in this direction.

## References

1. D.G. Eskin, Physical metallurgy of direct chill casting of aluminium alloys, *Advances in Metallic Alloys*, J.N. Fridlyander, Ed., CRC Press, Taylor & Francis Group, Boca Raton, 2008,
2. M. Stefanescu and R. Roxanda, *Solidification Structure of Aluminum Alloys*, The University of Alabama, Tuscaloosa, 2004
3. P. Jarry and M. Rappaz, Recent Advances in the Metallurgy of Aluminium Alloys, Part I: Solidification and Casting, *C. R. Phys.*, 2018, **19**, p 672–687
4. D. Brough and H. Jouhara, The Aluminium Industry: A Review on State-of-the-Art Technologies, Environmental Impacts and Possibilities for Waste Heat Recovery. *Int. J. Thermofluids*, 2020, **1–2**, p 100007
5. A. Pakanati, M. M'Hamdi, H. Combeau, and M. Zaloznik, Investigation of Macroseggregation Formation in Aluminium DC Casting for Different Alloy Systems, *Metall. Mater. Trans.*, 2018, **49A**(10), p 4710–4721
6. N. Bayat and T. Carlberg, Surface Formation in Direct Chill (DC) Casting of 6082 Aluminium Alloys, *Mater. Sci. Eng.*, 2016, **117**, p 012038
7. J. Sengupta, B.G. Thomas, and M.A. Wells, The Use of Water Cooling During the Continuous Casting of Steel and Aluminium Alloys, *Metall. Mater. Trans.*, 2005, **36A**, p 187–204
8. A.L. Greer, A.M. Bunn, A. Tronche, P.V. Evans, and D.J. Bristow, Modelling of Inoculation of Metallic Melts: Application to Grain Refinement of Aluminium by Al-Ti-B, *Acta Mater.*, 2000, **48**(11), p 2823–2835
9. Y. Birol, AlB3 Master Alloy to Grain Refine AlSi10Mg and AlSi12Cu Aluminium Foundry Alloys, *J. Alloys Compd.*, 2012, **513**, p 150–153
10. P. Jia, J.Y. Zhang, X. Hu, X.Y. Teng, M. Zuo, Z.R. Gao, C. Yang, and D.G. Zhao, Grain Refining Effects of the Melt Thermal-Rate Treatment and Al-Ti-B-Y Refiner in As-Cast Al-9Si-0.5 Mg Alloy, *Mater. Res. Express*, 2018, **5**, p 066520
11. A. Hellawell, S. Liu, and S.Z. Lu, Dendrite Fragmentation and the Effect of Fluid Flow in Casting, *JOM*, 1997, **49**(3), p 18–20
12. Y. Zuo, H. Nagaumi, and J. Cui, Study on the Sump and Temperature Field During Low Frequency Electromagnetic Casting a Superhigh Strength Al-Zn-Mg-Cu Alloy, *J. Mater. Process. Technol.*, 2008, **197**, p 109–115
13. Y. Zuo, J. Cui, Z. Zhao, H. Zhang, L. Li, and Q. Zhu, Mechanism of Grain Refinement of an Al-Zn-Mg-Cu Alloy Prepared by Low Frequency Electromagnetic Casting, *J. Mater. Sci.*, 2012, **47**, p 5501–5508
14. Y. Zuo, J. Cui, D. Mou, Q. Zhu, X. Wang, and L. Li, Effect of Electromagnetic Field on Microstructure and Macroseggregation on Flat Ingot of 2524 Aluminium Alloy, *Trans. Nonferrous Met. Soc. China*, 2014, **24**, p 2408–2413
15. B. Zhang, J. Cui, and G. Lu, Effects of Low-Frequency Electromagnetic Field on Microstructures and Macroseggregation of Continuous Casting 7075 Aluminum Alloy, *Mater. Sci. Eng. A*, 2003, **355**(1–2), p 325–330
16. H. Zhang Chen, H. Jiang, and J. Cui, Experimental Investigation of Macroseggregation in Low Frequency Electromagnetic Casting 7075 Aluminium Alloy, *Mat.-Wiss. U. Werkstofftech.*, 2011, **42**(6), p 500–505
17. H. Zhang, H. Nagaumi, Y. Zuo, L. Lei, and Q. Zhu, Coupled Modeling of Electromagnetic Field, Fluid Flow, Heat Transfer and Solidification During Low Frequency Electromagnetic Casting of 7XXX Aluminium Alloys Part I: Development of a Mathematical Model and Comparison with Experimental Results, *Mater. Sci. Eng. A*, 2007, **448**, p 189–203
18. H. Hao, X.G. Zhang, J.P. Park, H.Y. Kim, and J.Z. Jin, Twin-Strand Technology and Microstructure Analysis for the Electromagnetic Near Net-Shape Casting of Aluminium Alloy, *J. Mater. Process. Technol.*, 2003, **142**(2), p 526–531
19. Z. Zhao, J. Cui, J. Dong, and Z.B. Wang, Effect of Low-Frequency Magnetic Field on Microstructures of Horizontal Direct Chill Casting 2024 Aluminum Alloy, *J. Alloys Compd.*, 2005, **396**(1–2), p 164–168
20. Y. Zuo, J. Cui, J. Dong, and F. Yu, Effects of Low Frequency Electromagnetic Field on the As-cast Microstructures and Mechanical Properties of Superhigh Strength Aluminum Alloy, *Mater. Sci. Eng. A*, 2005, **408**, p 176–181
21. F. Wang, N. Wang, F. Yu, X. Wang, and J. Cui, Study on Micro-Structure, Solid Solubility and Tensile Properties of 5A90 Al-Li Alloy Cast by Low-Frequency electromagnetic Casting Processing, *J. Alloys Compd.*, 2020, **820**, p 153318
22. X.Y. Wang, J.T. Jiang, G.A. Li, X.M. Wang, J. Sun, and L. Zhen, Effects of Coarse Al<sub>2</sub>CuLi Phase on the Hot Deformation Behavior of Al-Li Alloy, *J. Alloys Compd.*, 2020, **815**, p 152469
23. R. Zhang, D. Wang, L. Huang, S. Yuan, and L. Geng, Deformation Behaviors and Microstructure Evolution of TiBw/TA15 Composite with Novel Network Architecture, *J. Alloys Compd.*, 2017, **722**, p 970–980
24. D.Z. Wang, R. Zhang, H. Yuan, and J. Qiang, Effect of Microstructure on the Hot Deformation Behavior of TiAl-Based Alloys Prepared by Powder Metallurgy Method, *JOM*, 2017, **69**(10), p 1824–1829
25. X.F. Ding, F.Q. Zhao, Y.H. Shuang, L.F. Ma, Z.B. Chu, and C.J. Zhao, Characterization of Hot Deformation Behavior of As-extruded AZ31 Alloy Through Kinetic Analysis and Processing Maps, *J. Mater. Process. Technol.*, 2020, **276**, p 116325
26. Z. Wan, L. Hu, Y. Sun, T. Wang, and Z. Li, Hot Deformation Behavior and Processing Workability of a Ni-Based Alloy, *J. Alloys Compd.*, 2018, **769**, p 367–375
27. S.H. Adarsh and V. Sampath, Hot Deformation Behavior of Fe-28Ni-17Co-11.5Al-2.5Ta-0.05B (at.%) Shape Memory Alloy by Isothermal Compression, *Intermetallics*, 2019, **115**, p 106632
28. J.H. Zhao, Y.L. Deng, J.G. Tang, and J. Zhang, Influence of Strain Rate on Hot Deformation Behavior and Recrystallization Behavior Under Isothermal Compression of Al-Zn-Mg-Cu Alloy, *J. Alloys Compd.*, 2019, **809**, p 151788
29. H.J. McQueen and W. Blum, Dynamic Recovery: Sufficient Mechanism in the Hot Deformation of Al, *Mater. Sci. Eng. A*, 2000, **290**(1–2), p 95–107



30. P.N. Crepeau, A.M. Gokhale, and C.W. Meyers, Quantitative Analysis of Cast Microstructures, *JOM*, 1989, **41**, p 16–21
31. G. Mrówka-Nowotnik, J. Sienawski, and M. Wierzbinska, Intermetallic Phase in 6082 Aluminium Alloy, *Arch. Mater. Sci. Eng.*, 2007, **28**(2), p 69–76
32. Y.L. Liu, S.B. Kang, and H.W. Kim, The Complex Microstructures in As-cast Al-Mg-Si Alloy, *Mater. Lett.*, 1999, **41**, p 267–272
33. M. Ahmedein, M. Wu, and A. Ludwig, Ludwig, Analysis of Macrosegregation Formation and Columnar-to-Equiaxed Transition During Solidification of Al-4 wt.%Cu Ingot Using a 5-Phase Model, *J. Cryst. Growth*, 2015, **417**, p 65–74
34. C. Hsu, K.A.Q. O'Reilly, B. Cantor, and R. Hamerton, Non-equilibrium Reactions in 6xxx Series Al Alloys, *Mater. Sci. Eng. A*, 2001, **304–306**, p 119–124
35. H.J. McQueen, T.G. Langdon, H.D. Merchant, J.-G. Morris, and M.A. Zaidi, *Hot Deformation of Aluminum Alloys*, TMS-AIME, Warrendale, PA, 1990, p 31–54
36. T. Sakai and C. Takahashi, Flow Softening of 7075 Aluminum Alloy Under Hot Compression, *Mater. Trans. JIM*, 1991, **32**(4), p 375–382
37. Y.C. Lin and X.M. Chen, A Critical Review of Experimental Result and Constitutive Description for Metals and Alloys in Hot Working, *Mater. Des.*, 2011, **32**, p 1733–1759
38. G.Z. Quan, G.S. Li, Y. Wang, W.Q. Lv, C.T. Yu, and J. Zhou, A Characterization for the Flow Behavior of As-Extruded 7075 Aluminum Alloy by the Improved Arrhenius Model with Variable Parameters, *Mater. Res.*, 2013, **16**(1), p 19–27
39. T. Sheppard and A. Jackson, Constitutive Equations for Use in Prediction of Flow Stress During Extrusion of Aluminium Alloys, *Mater. Sci. Technol.*, 1997, **13**, p 203–209
40. C.M. Sellars and G.J. Davies, Ed., *Hot Working and Forming Processes*, The Metals Society, London, 1980
41. C.M. Sellars, Modelling Microstructural Development During Hot Rolling, *Mater. Sci. Technol.*, 1990, **6**, p 1072–1081
42. H.J. McQueen and N.D. Ryan, Constitutive Analysis in Hot Working, *Mater. Sci. Eng. A*, 2002, **322**, p 43–63
43. C.M. Sellars and W. McTegart, On the Mechanism of Hot Deformation, *Acta Metall.*, 1966, **14**(9), p 1136–1138
44. S.F. Medina and C.A. Hernandez, General Expression of the Zener-Hollomon Parameter as a Function of the Chemical Composition of Low Alloy and Microalloyed Steel, *Acta Mater.*, 1996, **44**(1), p 137–148
45. C.W. Siyasiya and W.E. Stumpf, Constitutive Constants for Hot Working of Steels: The Critical Strain for Dynamic Recrystallization in C-Mn Steels, *J. Mater. Eng. Perform.*, 2015, **24**(1), p 468–476
46. C. Menapace, N. Sartori, M. Pellizzari, and G. Straffelini, Hot Deformation Behavior of Four Steels: A Comparative Study, *J. Mater. Sci. Technol.*, 2018, **140**(2), p 1–11
47. S. Spigarelli, E. Evangelista, and H.J. McQueen, Study of Hot Workability of a Heat Treated AA6082 Aluminum Alloy, *Scripta Mater.*, 2003, **49**, p 179–183
48. B. Zhang and T.N. Baker, Effect of the Heat Treatment on the Hot Deformation Behaviour of AA6082 Alloy, *J. Mater. Process. Technol.*, 2004, **153–154**, p 881–885
49. S. Wang, L.G. Hou, J.R. Luo, J.S. Zhang, and L.Z. Zhuang, Characterization of Hot Workability in AA 7050 Aluminum alloy Using Activation Energy and 3-D Processing Map, *J. Mater. Process. Technol.*, 2015, **225**, p 110–121

**Publisher's Note** Springer Nature remains neutral with regard to jurisdictional claims in published maps and institutional affiliations.